



Identification of champion transition metals centers in metal and nitrogen-codoped carbon catalysts for CO₂ reduction

Fuping Pan, Wei Deng, Carlos Justiniano, Ying Li*

Department of Mechanical Engineering, Texas A&M University, College Station, TX 77843, USA

ARTICLE INFO

Keywords:

Doped carbon
Transition metals
Iron
Nickel
CO₂ reduction

ABSTRACT

Transition metal is known to influence electrochemical activities over transition metals (M) and nitrogen (N)-codoped carbon (M–N–C) catalysts. However, champion transition metals centers in M–N–C for catalyzing CO₂ reduction reaction (CO₂RR) remain unclear, hindering further catalyst development with enhanced performance. Herein, we report the investigation of effects of five transition metals (Cr, Mn, Fe, Co, Ni) on CO₂RR activities and mechanisms using metal-doped nitrogenated carbon nanosheets as model catalysts fabricated via a novel space-confinement-assisted molecular-level complexing approach. Analyzing N 1s XPS spectra confirmed the formation of M–N complexes via the coordination of metals atoms with pyridinic N, which was identified as the active species in CO₂RR. According to activity descriptors including overpotentials, Faradaic efficiency (FE) and Turnover Frequency (TOF) per metal site, we here established that Fe and Ni are more active than Co, Mn, and Cr in M–N–C for the reduction of CO₂ to CO. The main role of Fe is to reduce overpotentials, exhibiting the lowest onset overpotential of 0.19 V to yield CO on Fe–N–C. Ni can drastically improve CO selectivity and reaction rates, yielding the highest CO Faradaic efficiency of 96%, partial current density of -8.2 mA cm^{-2} , and TOF of 1060 h^{-1} at a moderate overpotential of 0.65 V. Mechanism explorations reveal that CO₂RR on M–N–C (M = Fe, Cr, Mn) undergoes the formation of a ^{*}COOH intermediate as the rate-determining step, whereas M–N–C (M = Ni, Co) catalyzes CO₂RR via the transfer of the first electron to form a ^{*}CO₂^{•−} species. On the basis of the findings, we suggest doping Fe and/or Ni to design advanced M–N–C for CO₂ electroreduction.

1. Introduction

Growing global warming and energy demands have triggered a great interest in reusing the greenhouse gas CO₂ to reach an anthropogenic carbon cycle and utilizing renewable energy sources such as solar, wind and tidal to power human's activities. Room-temperature electrochemical CO₂ reduction by using water as a reaction medium and clean energy-generated electricity as the power input can not only convert CO₂ but also store intermittent renewable energy in value-added fuels simultaneously, which is believed to be one of the most attractive strategies to remit environmental and energy issues [1,2]. This desired technology, however, is technically hindered owing to the thermodynamically stable nature of CO₂ and the strong competition with hydrogen evolution reaction (HER) in aqueous electrolytes, leading to a prohibitive overpotential and a poor selectivity for CO₂ reduction reaction (CO₂RR) in practice [3,4]. Although selective electroreduction of CO₂ to CO and formic acid has been achieved, it requires the use of noble metals (Ag, Au, Pd) [5–7]. The core challenge of CO₂RR remains on the development of inexpensive, selective and stable

catalysts operating at low overpotentials.

Toward this goal, heat-treated transition metals (M) and nitrogen (N)-codoped carbon (M–N–C) catalysts have attracted numerous attention by virtue of their advantages including high CO₂-to-CO selectivity, rich reserve, chemical stability, and good conductivity [8–11]. Doping transition metals and nitrogen into the carbon matrix can break electroneutrality of carbons and increase charge and spin densities, thus transforming inert carbons into active electrocatalysts. So far, lots of M–N–C families, including Fe(Mn)/N-doped carbon black [12], N,P,Co-doped mesoporous carbon [13], Fe(Ni)/N-doped porous carbon [14,15] have been developed for CO₂RR to produce CO, in which nitrogen coordinated metal complexes (M–N) were proposed to be likely catalytic active sites owing to their optimal binding strength with the chemical species involved in CO₂RR [12,14–16]. Despite the reported advancements in the literature, M–N–C is still far from their practical applications due to poor activity, primarily suffering from large overpotentials and low currents [12–16]. Because different metals in M–N–C exhibit various behaviors in CO₂RR, it is imperative to identify the champion metal centers in M–N–C among various popular

* Corresponding author.

E-mail address: yingli@tamu.edu (Y. Li).

transition metals for CO₂ electroreduction. Nevertheless, the reported M–N–C catalysts functionalized by Fe, Co, Mn, and Ni were synthesized using various carbon/nitrogen precursors and different methods, resulting in huge differences in carbon architectures, metal species structures, and nitrogen doping level (contents and configurations) [12–15]. These discrepancies make it infeasible to identifying the most active metal center of M–N–C based on reported results because electrocatalytic activities of M–N–C are highly dependent on carbon structures, N/M chemical states and contents [14,17,18]. Moreover, the differences in CO₂RR pathways on different transition metals are not well understood, precluding the selection of most active M–N–C catalysts. Therefore, it is demanding to explore the electrocatalytic reactivity and behaviors of different transition metals in M–N–C, which will provide in-depth mechanistic understanding and guide the design of high-efficiency M–N–C electrocatalysts for CO₂ reduction by selectively doping M–N–C with the most efficient transition metal.

The objective of this paper is to identifying champion metals centers among five popular transition metals (Cr, Mn, Fe, Co, Ni) in M–N–C synthesized by the same method and understanding their specific catalytic roles in CO₂ reduction. Metal-doped nitrogenated carbon nanosheets were prepared by a space-confinement-assisted molecular-level complexing synthesis and studied as model catalysts. The structure, compositions, and nitrogen/metal chemical states were characterized by TEM, XRD, ICP-MS, and XPS. Electrochemical CO₂RR behaviors were then systematically evaluated and compared against undesired hydrogen evolution reaction. Catalytic properties including overpotentials, Faradaic efficiency, and turnover frequency per metal site for CO production were used as descriptors to rank the electrocatalytic reactivity of the five transition metals for CO₂ reduction. Moreover, Tafel analyses were performed to unveil electrocatalytic CO₂RR pathway, which provides mechanistic insights of the role of five metals on CO₂RR.

2. Experimental section

2.1. Synthesis of M–N–C

M–N–C was prepared via a simple solid-phase pyrolysis route. In a typical synthesis of Fe–N–C, urea (10 g), citric acid (0.334 g) and iron nitrate nonahydrate (0.035 g) were dispersed in deionized water (15 mL) with continuous stirring for 2 h and then dried at 80 °C to obtain a dried solid. The solid was ground into a uniform powder, which was put in a combustion boat and transferred into a tube furnace. Then, the temperature of the furnace was increased to 550 °C for 2 h and further raised to 900 °C for 1 h at a heating rate of 3 °C min^{−1} under argon flow. After cooling down to room temperature, final powder sample was collected. The iron contents and pyrolysis temperatures were adjusted to optimize CO₂RR activity of Fe–N–C; we found that 8.66×10^{-5} mol Fe in precursors and a heating temperature of 900 °C yielded the best CO₂RR activity (Fig. S1). Other M–N–C samples were prepared using the same procedure as for Fe–N–C except for employing different metal nitrate precursors but keeping the same metal content at 8.66×10^{-5} mol, and the metal-free N–C was synthesized using urea and citric acid as precursors for comparison purpose.

2.2. Physical characterization

Morphology, structure, and composition of catalysts were characterized by scanning electron microscopy (SEM, JEOL JSM7500F), transmission electron microscopy (TEM, FEI Tecnai G2 F20 ST), X-ray diffraction (XRD, BRUKER D8) and X-ray photoelectron spectroscopy (XPS, Omicron). Metal amounts in catalysts were determined by inductively coupled plasma mass spectrometry (ICP-MS, PerkinElmer NexION 300D Quadrupole); five replicates of each sample were analyzed to yield the average.

2.3. Electrochemical CO₂RR activity measurements

Electrocatalytic CO₂RR was evaluated in a two-compartment three-electrode electrochemical cell in CO₂-saturated 0.1 M KHCO₃ electrolyte (pH = 6.8). A Pt mesh and an Ag/AgCl (3 M KCl) were used as the counter electrode and reference electrode, respectively. The measured potentials after iR compensation were rescaled to the reversible hydrogen electrode by $E \text{ (RHE)} = E \text{ (Ag/AgCl)} + 0.210 \text{ V} + 0.0591 \text{ V} \times \text{pH}$. The working electrode was prepared by drop casting 60 μL of catalyst ink onto a carbon paper (1 cm²) with mass loading of 0.3 mg cm^{−2}. The ink was prepared by dispersing 3 mg catalysts in a mixture solution of 200 μL DI-water, 370 μL ethanol, and 30 μL 5% Nafion solution via sonication for 3 h. The working and reference electrodes were placed in the cathode chamber, while the counter electrode was placed in the anode chamber, which was separated by a piece of Nafion 115 ionic exchange membrane to avoid the re-oxidation of CO₂RR-generated products. The high-purity CO₂ was introduced in the cathode chamber for 1 h to saturate electrolyte before electrolysis with a flow rate of 34 mL min^{−1} and maintained this flow rate during measurements. The gas-phase products were analyzed via an online gas chromatograph (GC, Fuel Cell GC-2014ATF, Shimadzu) equipped with a thermal conductivity detector (TCD) and a methanizer assisted flame ionization detector (FID). The GC calibration is provided in Supporting Information. The liquid-products were characterized by a nuclear magnetic resonance (NMR) spectrometer (Bruker avance III 500 MHz). 2,2,3,3-d(4)-3-(trimethylsilyl)propionic acid sodium salt (TSP) was used as the internal standard, and the 0.6 mM TSP standard solution was prepared in D₂O [19]. The representative sample for ¹H NMR was prepared by depositing 500 μL of the KHCO₃ solution collected after 550 min CO₂RR tests on Ni–N–C at −0.75 V in an NMR tube followed by adding 100 μL of STP standard solution.

The activity descriptors including Faradaic efficiency (FE), partial current density, mass activity, production rates, and turnover frequency (TOF) per metal site for CO production were calculated to reveal the catalytic properties, and the calculation methods are provided in Supplementary Materials.

3. Results and discussion

3.1. Synthesis, structure, and composition of M–N–C

Since previous reports have suggested that M–N species serves as primary active sites in CO₂RR [12,14], the preparation of M–N–C with high-density M–N dopants is thereby the premise to compare their CO₂RR activities. In this work, we synthesized metal/nitrogen-doped carbon nanosheets as presenting M–N–C by atomically constructing the M–N coordination via a molecular-level complexing chemistry design with space-confinement assistance. As depicted in Fig. 1a, citric acid, urea, and metal nitrate were used as starting feedstock, and a solid-phase pyrolysis route was carried out to fabricate M–N–C. Citric acid was the carbon precursor, which also served as the complexing agent to chelate the transition metals in water because of its high affinity to metal ions [20,21], guaranteeing a uniform dispersion of the metals species. During the carbonization at 550 °C, urea surrounding around citric acid-metal composites polycondensed into layer-structured graphitic carbon nitride (g-C₃N₄), which thus functioned as a space-confined nanoreactor to direct the formation of two-dimensional graphene-like carbon and further hindered the aggregation of the metals species due to space-limited effects from g-C₃N₄ interlayers [22,23]. When the temperature reached 750 °C, the decomposition of thermally unstable g-C₃N₄ templates liberated carbon nanosheets. In the meantime, numerous nitrogen-containing gases (NH₃, C₂N₂⁺, C₃N₂⁺, C₃N₃⁺) were generated during the process of the thermolysis of urea and g-C₃N₄ [24,25], which provided rich nitrogen sources to react with carboxyl/hydroxy of carbon intermediates and substitute carbon atoms, leading to the formation of the M–N complexes and other C–N and O–N groups.

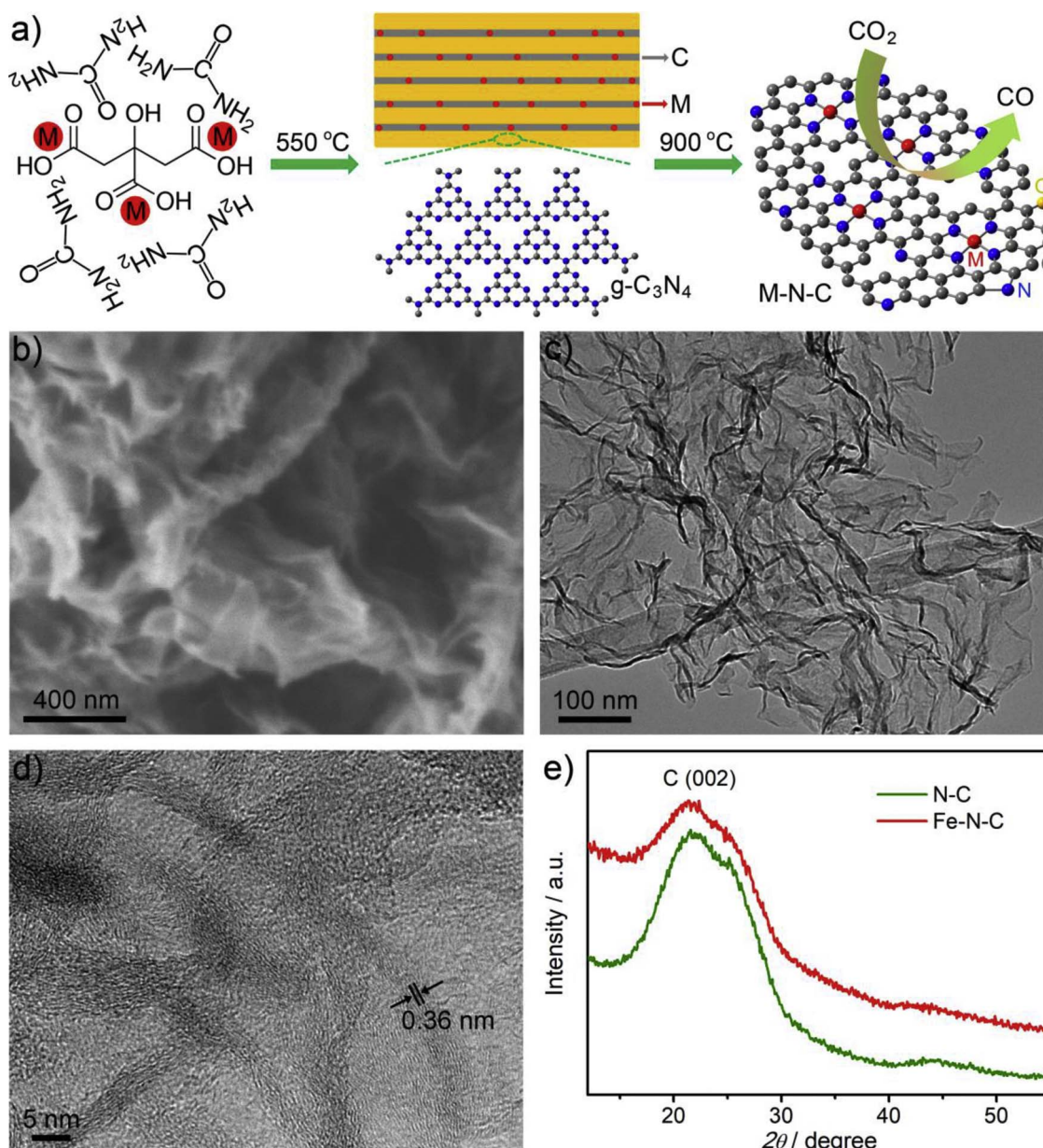


Fig. 1. (a) Schematic illustration of the fabrication process for M-N-C. (b) SEM, (c) TEM and (d) HRTEM images of Fe-N-C. (e) XRD patterns of N-C and Fe-N-C.

The morphology of Fe-N-C was characterized by scanning electron microscopy (SEM) and transmission electron microscopy (TEM). An SEM image in Fig. 1b shows that Fe-N-C consisted of wrinkled and entangled flakes. This can be further confirmed by a TEM image in Fig. 1c, presenting cross-linked and transparent ultra-thin graphene-like features, similar to morphology of the counterpart of “metal-free” N-doped carbon nanosheets (N-C) (Fig. S2). From a high-resolution TEM image in Fig. 1d, long-range contorted stripes of about 5 nm in thickness and of 0.36 nm in interlayer distance were observed, directly demonstrating curved few-layered graphene. The atomic layers structure is derived from the duplication of layered-structured g-C₃N₄ templates, and the crumpled characteristic could be ascribed to the local stress induced by lattice defects (nitrogen and iron dopants) and to the blowing effects induced by numerous gases [26,27]. Fig. 1e shows X-ray Diffraction (XRD) patterns of Fe-N-C and N-C. XRD data of other M-N-C are presented in Fig. S3. All samples exhibited same polycrystalline graphitic characteristics with an obvious broad peak of graphitic (002) plane. No particles in TEM images and crystallographic features in XRD patterns indicate that metal atoms might exist in an

atomically dispersed state confined in the carbon layers.

The actual metals contents in M-N-C were determined by inductively coupled plasma mass spectrometry (ICP-MS), which are 2.14, 2.83, 2.52, 2.22, and 2.74 wt.% for Fe, Ni, Co, Cr, and Mn in M-N-C, respectively. Note that the metal concentrations in M-N-C are at the same level with only small variations (2.49 ± 0.30 wt.%). The metal content in the N-G catalyst without the addition of metal precursors was found to be 0.06 wt.%, which is negligible compared to that in M-N-C. We further conducted X-ray photoelectron spectroscopy (XPS) to investigate surface N contents and chemical states of doped atoms. XPS survey spectra are depicted in Fig. S4, in which the presence of C, N, O in all catalysts as well as metals in M-N-C can be verified, suggesting the successful doping of N and metals in the carbon matrix. The total N atomic contents are summarized in Table 1 (in Supplementary material). The N content of N-C is 12.23 at.%, close to those of M-N-C. This is probably due to the fact that the N doping process is mainly determined by the carbon/nitrogen precursors and heating temperature [28]; the same synthetic recipes thus result in a close N doping level in N-C and M-N-C.

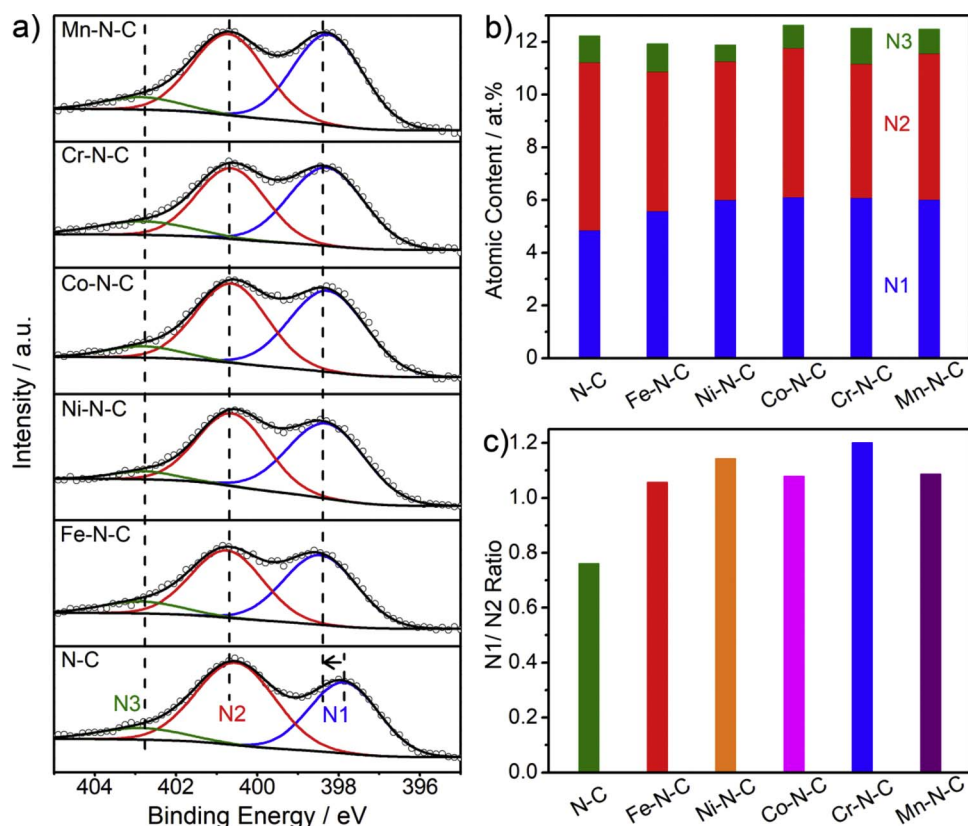


Fig. 2. (a) High-resolution N 1s spectra, (b) Atomic contents of different N species, and (c) N1:N2 atomic ratio of N–C and M–N–C. N1, N2, and N3 refer to pyridinic, graphitic, and oxidized N, respectively.

High-resolution metals $2p_{3/2}$ XPS spectra of M–N–C were further deconvoluted to analyze their chemical states. As shown in the fitted Fe $2p_{3/2}$ spectrum (Fig. S5a), two main peaks centered at 709.6 eV and 711.5 eV are assigned to Fe^{2+} and Fe^{3+} , respectively, coupled with a satellite peak at 717.8 eV [29–31]. As for Ni, a typical peak at 854.8 eV is indicative of the formation of Ni^{2+} in Ni–N–C (Fig. S5b) [32]. Fig. S5c presents Co $2p_{3/2}$ spectrum, which can be well split into a main peak at 780.4 eV and two satellites peaks at higher binding energies. The peak of 780.4 eV suggests the existence of Co^{2+} ions in Co–N–C [33]. The Cr $2p_{3/2}$ spectrum features at a dominating peak at 576.5 eV (Fig. S5d), which is ascribed to the Cr^{3+} ; Cr^{4+} may also exist as it is hard to distinguish Cr^{3+} from Cr^{4+} attributed to their similar binding energies [34,35]. The Mn $2p_{3/2}$ spectrum showed two peaks at 641.5 and 645.9 eV (Fig. S5e), corresponding to Mn^{3+} and satellite, respectively [36]. Based on reported XPS binding energy results for metallic phases of these five metals [37], we labeled binding energy positions of M^0 in XPS spectra. As can be seen in Fig. S5, all obtained metal $2p_{3/2}$ spectral profiles of M–N–C are significantly positive than those of M^0 (706.6 eV for Fe^0 , 852.6 eV for Ni^0 , 778.1 eV for Co^0 , 574.2 eV for Cr^0 , and 638.5 eV for Mn^0) [37], implying that no M^0 was formed or their contents might be extremely low. These observations are in good agreement with reported findings that transition metals commonly exist in the form of M^{2+} and M^{3+} in M–N–C catalysts when M^0 was not detected [15,29,33,38,39]. Combined with TEM and XRD characterizations, it is thus assumed that these five transition metals are mainly in the form of non-metallic phases dispersed in N-doped carbon.

Recent findings have demonstrated that transition metals ions can coordinate with N atoms (especially pyridinic N) during the thermal carbonization of the mixture composed of transitions metals, nitrogen, and carbon precursors and generate the M–N complexes [12,15,33,40], which are considered as determining catalytic species in CO2RR [12,14–16]. In addition, the evolution of M–N species via bonding between metal atoms and N atoms can lead to the change in the

electronic environment of N atoms compared with “metal-free” N-doped counterpart. This change can be directly verified by comparing N 1s XPS spectra, which have been used as a criterion to verify the generation of the M–N complexes [41–43]. Thereby, the high-resolution N 1s XPS spectra of N–C and M–N–C were further analyzed to reveal the formation of the M–N complexes. It has been widely accepted that N doping can occur either via substituting carbon atoms in the graphitic structure or reacting between gaseous N-based sources with oxygen-containing functionalities of carbon, which commonly leads to the formation of edge-like pyridinic N, five-membered heterocyclic rings-like pyrrolic N, bulk-like graphitic N, and oxidized N with N–O bonds [28,44–46]. As presented in Fig. 2a, there are two distinct peaks for all samples, where the peak at binding energy lower than 398.5 is assigned to pyridinic N (N1) and the peak located at 400.7 eV corresponds to graphitic N (N2) [46,47]. The deconvoluted peak at a higher binding energy of 402.8 eV can be attributed to oxidized N (N3), which accounts for a small proportion [28]. Previous reports demonstrated that pyrrolic N is commonly centered at around 399.5 eV [28,48]; however, we do not observe the presence of an obvious peak at about 399.5 eV, suggesting that pyrrolic N may not be formed or its content is extremely low. We thus neglected pyrrolic N in the fitted N 1s spectra in the revised manuscript, agreeing with some literature that pyrrolic N was commonly not included owing to its low contents [42,44,47].

Notably, the pyridinic N position in N–C centered at 397.8 eV is positively shifted to 398.5 eV in M–N–C with a binding energy value increase of 0.7 eV, while the position of graphitic N (400.7 eV) shows no difference between N–C and M–N–C, implying that only the chemical environment of pyridinic N is changed when metals are incorporated into N–C (Fig. 2a). The positive shift of pyridinic N with the addition of metals can be attributed to the formation of bonding between pyridinic N and metals. This is in good agreement with the reported findings that the binding energy of pyridinic N will shift to a higher value when a chemical bond between metal and N is formed and

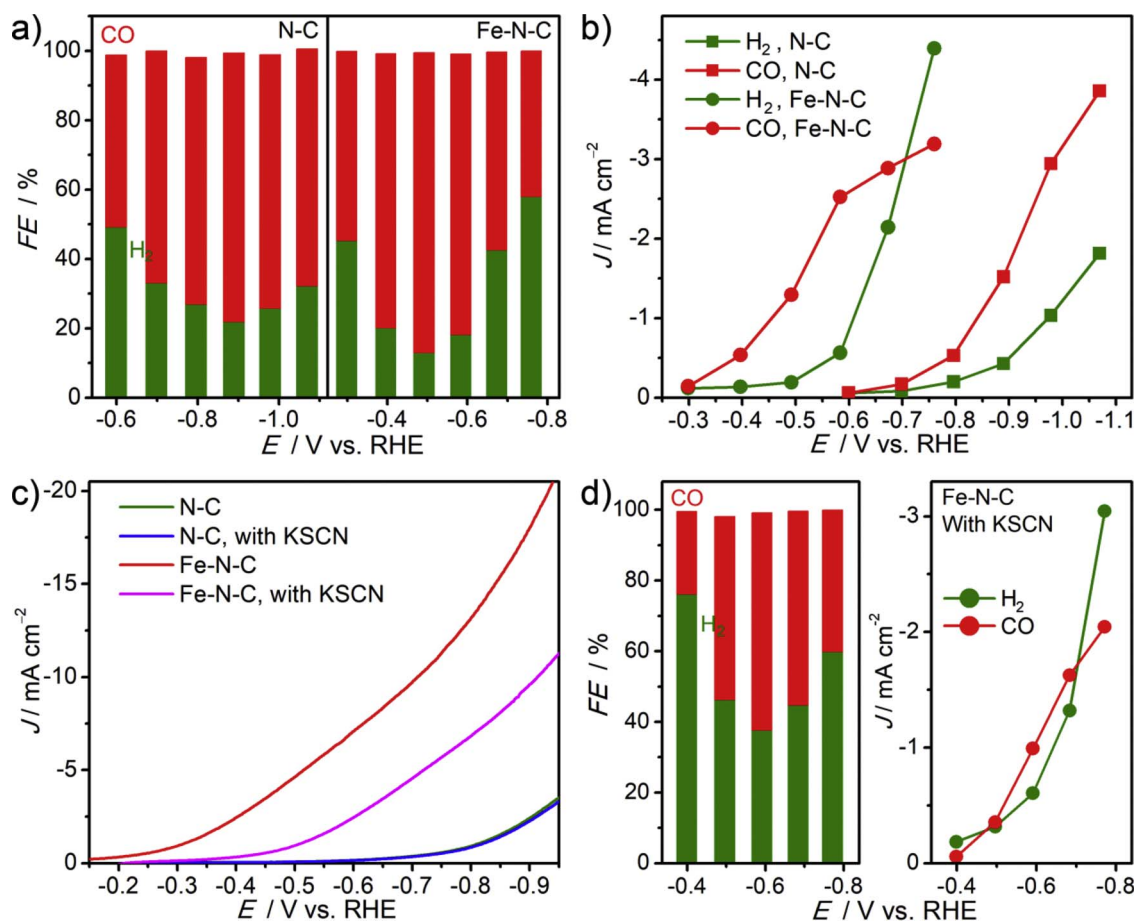


Fig. 3. (a) FEs and (b) Partial current densities for CO and H₂ of N-C and Fe-N-C at different applied potentials in CO₂-saturated 0.1 M KHCO₃. (c) Linear sweep voltammetry of N-C and Fe-N-C in the presence and absence of 0.01 M KSCN at a scan rate of 5 mV s⁻¹. (d) FEs and partial current densities for CO and H₂ of SCN⁻ poisoned Fe-N-C.

that metals ions preferentially coordinate with pyridinic N rather than graphitic N due to the existence lone-pair electron on pyridinic N [42,49]. The increase in the pyridinic N binding energy can be ascribed to the introduction of an ion withdrawing effect when a proton on pyridinic N was replaced by a metal ion [43,50]. Thereby, it is concluded that metals atoms in M-N-C may mainly coordinate with pyridinic N, leading to the formation of M-N sites. Moreover, benefiting from the well-dispersed metal species without metallic phases in M-N-C, it is believed that the metal atoms are uniformly distributed in the carbon matrix, which might be conducive to the formation of the M-N complexes and eventually maximize the density of the M-N complexes. However, such small difference in binding energy of pyridinic N and M-N coordination prevents further deconvolution to calculate the contents of the M-N complexes [48,51]. Here, the atomic contents of N species are calculated based on the peak area. As shown in Fig. 2b,c and Table 1 (in Supplementary material), despite M-N-C and N-C have similar total N contents, pyridinic N contents in M-N-C are higher than that of N-C, as also evidenced by relatively higher peak intensity of pyridinic N in M-N-C compared to that in N-C. This suggested that M incorporation benefits the formation of pyridinic N, which might be because more N sources interact with M during the M-N-C synthesis process. On the other hand, it was noted that all five M-N-C catalysts exhibited similar atomic contents of these three N groups and N configurations. Since N- and M-induced species mainly act as catalytic centers in CO₂ reduction, the same N doping level and structure will not cause interferences on the exploration of the reactivity order for the transition metals via comparing CO selectivity and specific activity between these five M-N-C catalysts with known metals amounts.

3.2. Catalytic origin of Fe-N-C for CO₂RR

Prior to investigating the reactivity sequence of the transition metals in M-N-C, it is imperative to confirm their contributions to CO₂RR. As Fe-N-C is a well-studied CO₂RR electrocatalyst, we here selected Fe-N-C as a model to probe the role of the metals in CO₂ reduction, and metal-free N-C was measured in the same condition as a reference. We observed that H₂ and CO are main products with tiny CH₄ (Fig. S6), accounting for a total FE of more than 98%. As shown in Fig. 3a, CO₂RR on N-C started at -0.60 V with a CO FE of 50%, and a maximum CO FE of 78% was obtained at -0.89 V, corresponding to an overpotential of 0.78 V because the CO₂/CO equilibrium potential is 0.11 V vs. RHE [6]. Notably, Fe-N-C showed the occurrence of CO₂RR at -0.3 V with a CO FE of 53%, which reached to a maximum FE of 87% at an overpotential of 0.38 V. This is 400 mV more positive than that of N-C. In addition, CO current densities normalized by the geometrical electrode area of Fe-N-C are much larger than those of N-C at the same potentials (Fig. 3b). These results clearly confirm the important roles of Fe in CO₂ reduction, which lowers overpotentials, enhances selectivity and increases reaction rates (that is, current) for the CO production. To further verify the Fe role, a control experiment of employing SCN⁻ as a probing agent was conducted since SCN⁻ ion has a high affinity to iron and can poison the Fe-N coordination site, while SCN⁻ does not have an impact for N-C [52]. Fig. 3c depicts LSV curves of N-C and Fe-N-C in the presence and absence of KSCN, indicating that Fe-N-C exhibited a drastic decrease in currents after adding KSCN owing to the blocking of the Fe center, whereas LSV curves of N-C remained unchanged with KSCN. Furthermore, poisoned Fe-N-C showed a maximum CO selectivity of 62% at -0.59 V; this is much

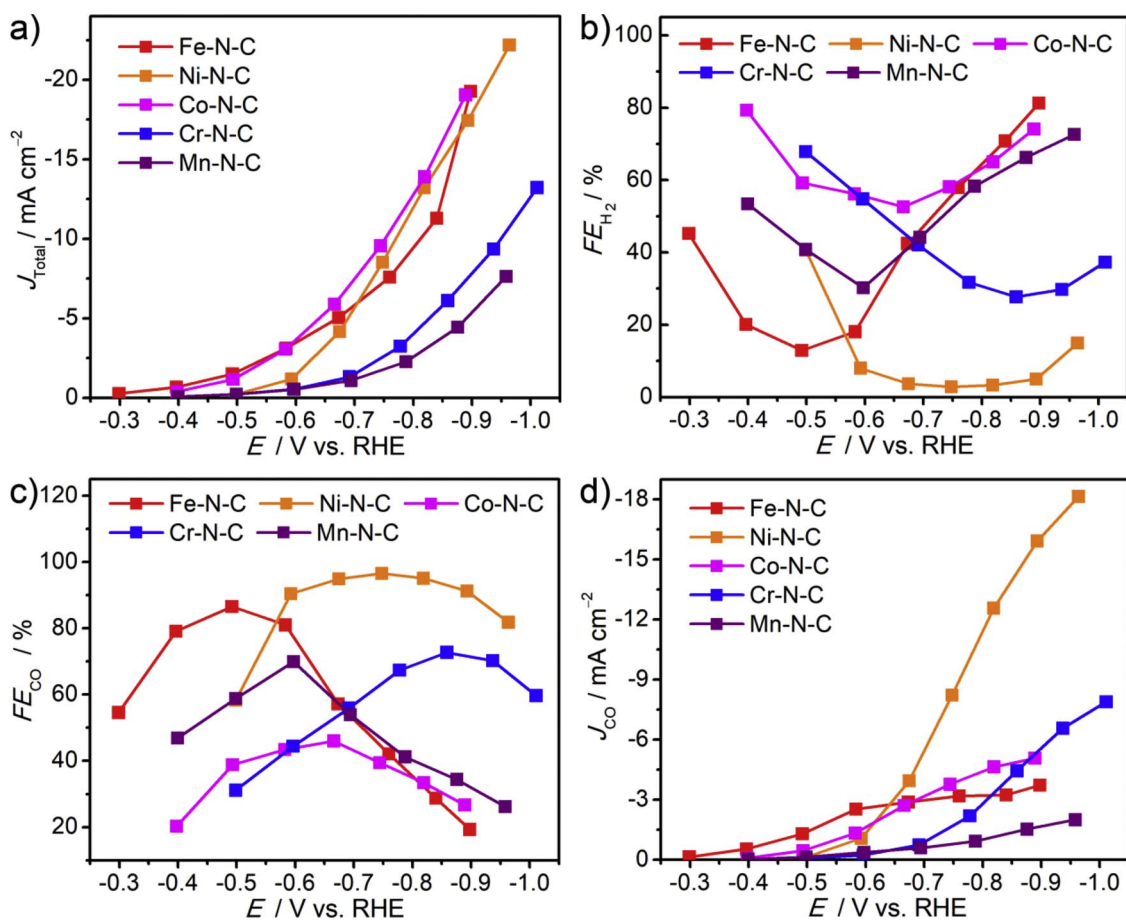


Fig. 4. (a) Total current densities, (b) H₂ FEs, (c) CO FEs, and (d) CO partial current densities for M-N-C.

lower than that of fresh Fe-N-C (87% at -0.49 V), accompanied by a decline in CO currents and an increase in H₂ FEs at overall potentials (Fig. 3d). These findings clearly reveal that enhanced CO₂RR performance of Fe-N-C is as a result of the intrinsically active nature of the Fe-N center.

3.3. Electrochemical CO₂RR behaviors of M-N-C

Electrochemical activities of series M-N-C (M = Cr, Mn, Fe, Co, Ni) for CO₂ reduction were further examined. Fig. 4a depicts the total current density of M-N-C at different applied potentials. Among them, Fe(or Co, Ni)-M-N-C showed overall currents approaching 20 mA cm⁻² at about -0.9 V, which are much larger than those of Mn-N-C and Cr-N-C. Compared to N-C, all M-N-C exhibited higher total currents (Fig. S7), demonstrating that the metal doping enhances reaction rates of N-C in CO₂ reduction. To determine the selectivity of products on M-N-C, FEs for H₂ and CO were calculated. As shown in Fig. 4b,c, volcano-like curves of CO FEs as a function of applied potentials were observed, while H₂ showed opposite tendency. This implies a potential-dependent characteristic for H₂ and CO production and the competitive nature of CO₂RR reduction and HER [14]. Notably, among series M-N-C, Fe-N-C and Ni-N-C were found to have higher CO FEs compared to N-C. These results suggest that Fe(or Ni)-N possesses a better capability in increasing selectivity for catalyzing CO₂RR to CO than metal-free C-N dopants. As can be seen from CO partial current densities in Fig. 4d, Fe-N-C showed the highest CO currents under more positive potentials regions (> -0.58 V), while Ni-N-C presented the highest CO currents at potentials of < -0.75 V.

In specific, Fe-N-C exhibited the smallest onset overpotential of about 0.19 V with CO FE of 53%, and a maximum CO FE of 87% was

achieved at an overpotential of 0.38 V (Fig. 4c). However, it had a relatively low current of -1.3 mA cm⁻² (mass activity of -4.3 mA g⁻¹) at an overpotential of 0.38 V (Fig. 4d, Fig. S8), corresponding a CO production rate of 0.024 mmol cm⁻² h⁻¹ (Fig. 5a). This implies that Fe has the best ability to reduce the CO₂-to-CO overpotential compared to others. As for Ni-N-C, it exhibited the highest CO FE of 96% at an overpotential of 0.64 V, suggesting that Ni is the best metal to suppress hydrogen evolution and eventually improve CO selectivity (Fig. 4b). In addition, at overpotential of 0.64 V, the CO current and production rate reached -8.2 mA cm⁻² (mass activity of -27.4 mA g⁻¹) and 0.15 mmol cm⁻² h⁻¹, respectively, which are significantly higher than others at the same overpotential. Upon Co-N-C, although it delivered the lowest CO FE of 46% at an overpotential of 0.56 V because Co preferred to reduce protons to H₂ (Fig. 4b), it showed a moderate overpotential lower than that of Ni-N-C and a decent CO current (-2.7 mA cm⁻², -9.0 mA g⁻¹) larger than that of Fe-N-C. Mn-N-C was found to show a lower overpotential (0.49 V) than those of other metals except Fe (110 mV larger than that of Fe-N-C) to reach a maximum FE of 70%. The shortage of Mn-N-C is that it possessed the lowest CO currents and mass activities at all potentials regions (Fig. 4d, Fig. S8), meaning inferior CO production rates (Fig. 5a). Cr-N-C showed a comparable maximum CO FE relative to Mn-N-C (72% vs. 70%), whereas the overpotential of Cr-N-C required to reach maximum CO selectivity is 260 mV larger than that of Mn-N-C.

3.4. Reactivity order of the transition metals in M-N-C toward CO₂RR

Since metals-containing species (in particular, M-N complexes) plays determining roles in CO₂ reduction, we thus further calculated CO TOF per metal site to reveal catalytic properties for these five metals. As

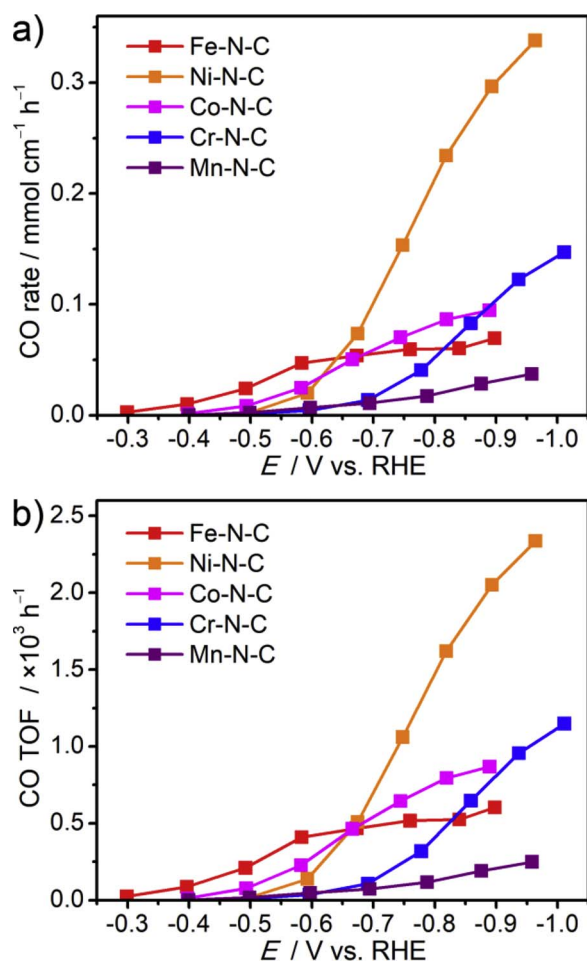


Fig. 5. CO production rates and CO TOFs of M–N–C at different potentials.

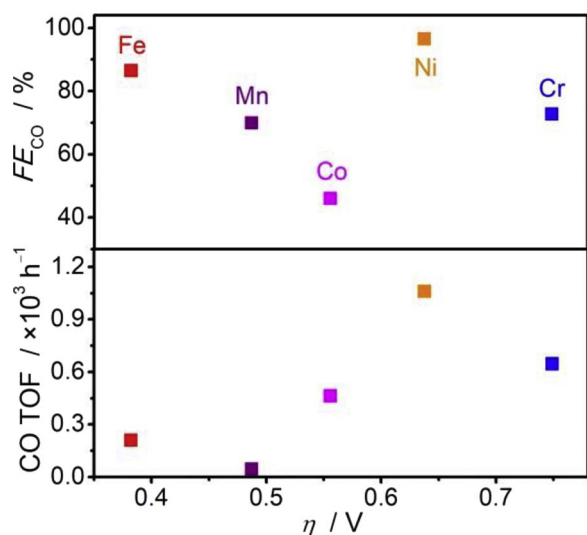


Fig. 6. Summary of maximum CO FEs and CO TOFs at corresponding overpotentials for M–N–C.

shown in Fig. 5b, when applied potentials are positive than -0.58 V, Fe–N–C showed the highest TOFs. For example, at -0.58 V, CO TOFs follow the order of are Fe–N–C (410 h^{-1}) > Co–N–C (230 h^{-1}) > Ni–N–C (140 h^{-1}) > Mn–N–C (46 h^{-1}) > Cr–N–C (35 h^{-1}). At potentials more negative than -0.75 V, CO TOFs of Co–N–C, Ni–N–C and Cr–N–C increase drastically, while Fe–N–C and Mn–N–C exhibited slow increases in CO TOFs. Notably, Ni–N–C

delivered a TOF of 1060 h^{-1} at an overpotential of 0.64 V and a TOF of 2338 h^{-1} at an overpotential of 0.85 V, which are substantially higher relative to those of other M–N–C.

To gauge the reactivity order of the transition metals, the overall performance including overpotential, FEs, and TOFs were considered as it is highly desirable that CO₂ reduction could occur at a low overpotential while maintaining high CO selectivity and reaction rate per catalyst site. We then summarized the maximum achievable CO FEs and CO TOFs at corresponding overpotentials for these five M–N–C catalysts (Fig. 6). It is obvious that, among series, Fe–N–C showed the lowest overpotential of 0.38 V to reach maximum FE of 87% and Ni–N–C showed the highest FE of 96% and the highest TOF of 1060 h^{-1} at a moderate overpotential of 0.64 V, which are much better than others. Combined with above CO₂RR behaviors discussions, it is concluded that Fe and Ni are intrinsically efficient metals in M–N–C for the reduction of CO₂ to CO, while Mn, Co, and Cr possess lower properties in catalyzing CO₂ reduction compared to Fe and Ni.

3.5. CO₂RR mechanisms on M–N–C

Active sites of N-doped carbon in CO₂RR have been suggested to be positively charged carbon atoms adjacent to nitrogen atoms, which can absorb CO₂ and stabilize intermediates [11,53–55]. For M–N–C, CO₂RR mainly occurs on M–N sites because transition metals play more significant roles as primary centers in stabilizing CO₂RR-involved intermediates [12,14–16]. To gain further insight into electrokinetic mechanisms of CO₂ reduction on M–N–C, Tafel analyses were performed. The Tafel slope (b) is given by the partial derivative of overpotentials (η) with respect to the log of CO currents (J_{CO}) as follows [56,57]:

$$b = \frac{\partial \eta}{\partial \log J_{\text{CO}}}$$

The correlation between Tafel slope and electron transfer coefficient (α) can be written as: [53,56,57]

$$\alpha = \frac{2.3RT}{bF}$$

where F is Faraday constant, R is the gas constant, T is the absolute temperature.

Here, Tafel plots (overpotentials as a function of the log of CO current densities) of M–N–C are shown in Fig. 7a, which indicates the presence of linear regions at low overpotentials for all samples. From the fitted slope results in Fig. 7b, it is obvious that Ni–N–C exhibited the lowest Tafel slope of 118 mV dec^{-1} , followed by Co–N–C (147 mV dec^{-1}), Cr–N–C (186 mV dec^{-1}), Mn–N–C (196 mV dec^{-1}), and Fe–N–C (200 mV dec^{-1}). According to the relationship between Tafel slope and electron transfer coefficient, Tafel slopes of 118 and 147 mV dec^{-1} correspond to electron transfer coefficient of 0.5 and 0.4 , respectively. Based on the Butler-Volmer theory [58,59], an electron transfer coefficient close to 0.5 means that the initial transfer of the first electron is the rate-determining step in an electrochemical reaction. Previous results including Tafel slopes of 110 mV dec^{-1} on Cu nanowires and 133 mV dec^{-1} on polycrystalline Ag also confirmed that the formation of a $^* \text{CO}_2^-$ intermediate through a one-electron transfer to a CO₂ molecule is the rate-determining step. Due to their comparable Tafel slopes, we propose that CO₂ reduction on Ni–N–C and Co–N–C proceeds through a rate-determining transfer of one electron to CO₂ to generate the surface adsorbed $^* \text{CO}_2^-$. Subsequently, the $^* \text{CO}_2^-$ combines with another electron and two protons, forming adsorbed $^* \text{CO}$ and H₂O, followed by the desorption of CO (Fig. 7c). As for Cr–N–C, Mn–N–C and Fe–N–C, they showed larger Tafel slopes around 200 mV dec^{-1} . This value means that the electron transfer coefficient is largely deviated from 0.5 . In this case, the rate-determining rate may be governed by the simultaneous occurrence of an electron transfer process and a reactant-involved chemical process [60].

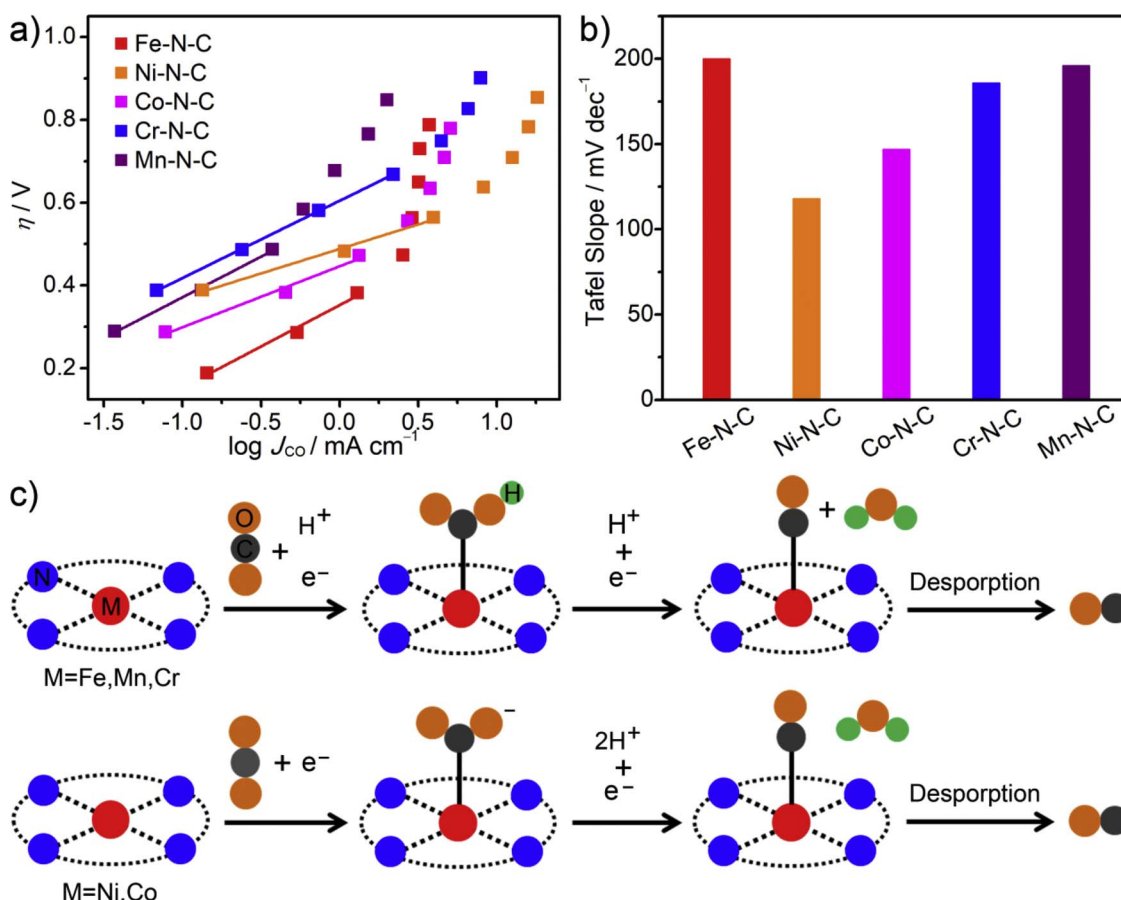


Fig. 7. (a) Tafel plots of CO current densities vs. overpotentials M–N–C. (b) Corresponding Tafel slopes obtained from (a). (c) Proposed CO₂RR mechanisms on M–N–C.

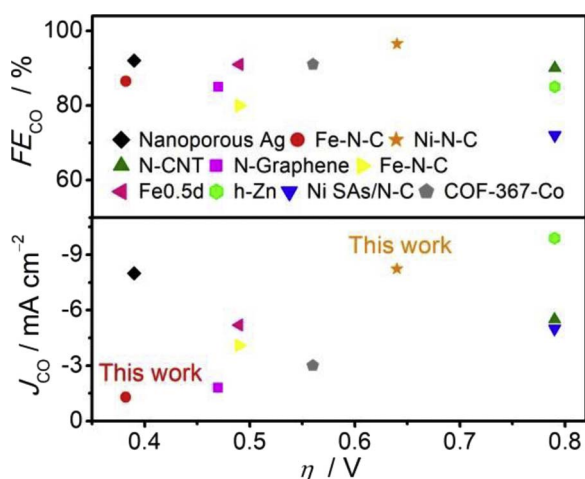


Fig. 8. Comparisons of CO FEs, partial current densities and corresponding overpotentials of Fe–N–C and Ni–N–C with those of reported typical electrocatalysts: nanoporous Ag [6]; N–CNT [53]; N–graphene [65]; Fe–N–C [12]; Fe0.5d [14]; h–Zn [66]; Ni SAs/N–C; [15] and COF-367-Co [67].

It has been proposed that a proton-coupled electron transfer process may take place in the CO₂ reduction [57,61], in which the formation of a *COOH intermediate via the electron-proton-transfer reaction for CO₂ activation is assumed as the rate-determining step. Previous experimental studies on N-doped carbon nanotube with a Tafel slope of about 200 mV dec^{-1} matched well with the theoretical prediction that proton-coupled electron transfer process with *COOH intermediate took place in the CO₂ reduction [62]. In our case, Tafel slopes of Fe(or Mn, Cr)–N–C are close to as-prepared N–C (Fig. S9) and reported N–

doped carbon nanotube [62]. Similar Tafel slopes thus suggest that CO₂RR on Fe–N–C may undergo the protonation of CO₂ to the *COOH intermediate as the rate-determining step; the *COOH further reacts with another one electron and one proton to form adsorbed *CO and H₂O, followed by the desorption of CO (Fig. 7c). This mechanism may also work on Mn–N–C and Cr–N–C due to similar Tafel slopes. The various mechanisms of these five transition metals in M–N–C toward CO₂RR may be attributed to their different electronic properties that lead to huge differences in binding strength between M–N sites and CO₂/intermediates [63,64].

3.6. Activity comparisons and electrochemical stability

To figure out the activity level of our catalysts, their activities were compared with many state-of-the-art CO₂RR electrocatalysts reported in literature. As can be seen in Fig. 8, an achievable maximum CO FE (87%) of Fe–N–C in this work is slightly smaller than that of noble nanoporous Ag (92%); however, they exhibited similar overpotentials (0.38 vs. 0.39 V) [6], despite Fe–N–C had a lower CO current (-1.3 mA cm^{-2} vs. -8 mA cm^{-2}). As for Ni–N–C, it showed a higher maximum CO FE (96%) and a comparable CO current density (-8.2 mA cm^{-2}) to nanoporous Ag. The main drawback of Ni–N–C relative to Ag is that it required a 250 mV higher overpotential to reach the highest FE. When comparing with non-precious catalysts such as N-doped carbon nanotube (N–CNT) [53], N-doped graphene [65], NFe-doped carbon [12,14], hexagonal Zn [66], NNi-doped MOF-derived carbon [15], and Co-based covalent organic frameworks (COF-367-Co) [67], our Fe–N–C showed the lowest overpotential to reach comparable FEs, and Ni–N–C exhibited outstanding advantages of having the highest CO FE and an enhanced current under a moderate overpotential. Thus, as-prepared Fe–N–C and Ni–N–C are in fact one of

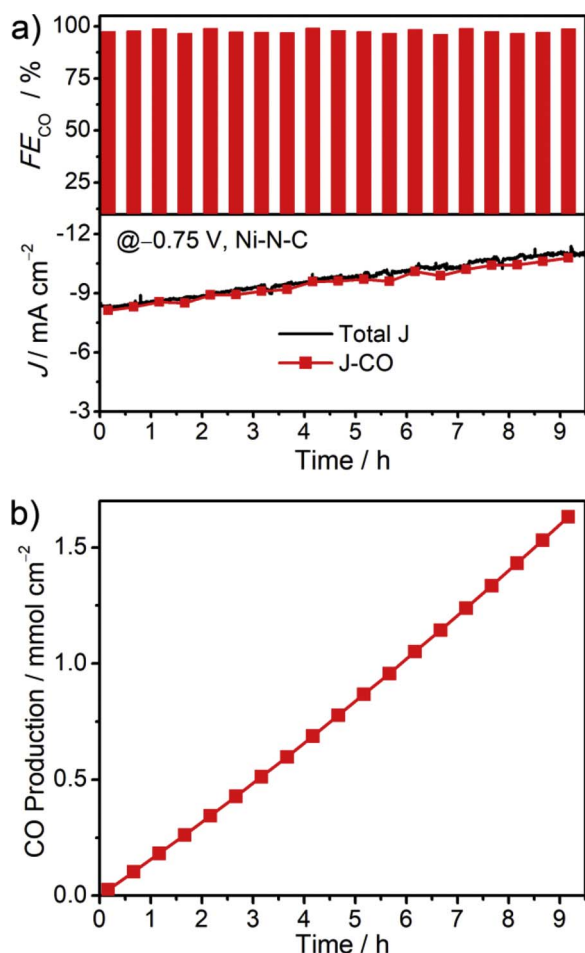


Fig. 9. (a) Long-term stability of Ni–N–C at -0.75 V. (b) Total production of CO on Ni–N–C in 550 min of continuous tests.

the best electrocatalysts reported so far for the electrolysis reduction of CO_2 to CO.

Apart from activity, electrochemical stability is another important criterion to evaluate the performance of an advanced electrocatalyst. Here, Ni–N–C was subjected to performing long-term CO_2 reduction at -0.75 V. As shown in Fig. 9, stable CO FEs over 96% were maintained without a decrease in CO currents, signifying remarkable electrochemical stability. A total CO production of $1.63 \text{ mmol cm}^{-2}$ was obtained in 550 min continuous tests, and no liquid product was detected (Fig. S10).

4. Conclusion

In summary, we have fabricated series of M–N–C ($\text{M} = \text{Cr}, \text{Mn}, \text{Fe}, \text{Co}, \text{Ni}$) by a molecular-level complexing with space-confinement assistance approach, which were applied as the model catalysts to explore the effects of the transition metals in M–N–C for CO_2 electroreduction. Experimental studies using SCN^- ion poisoning reveal that the M–N complex is the active site in CO2RR. The investigation of overall CO2RR performance established that Fe and Ni are intrinsically more active than Mn, Co, and Cr in M–N–C for the reduction of CO_2 to CO. The primary role of Fe was identified to reduce the overpotential, while Ni can significantly improve CO selectivity and boost reaction rates. Tafel analyses demonstrated that Fe in M–N–C catalyzes CO2RR through coupled electron-proton-transfer to form a $^*\text{COOH}$ intermediate as the rate-determining step, whereas the rate-determining step toward CO2RR on Ni–N–C involves the initial transfer of the first electron to form a $^*\text{CO}_2^{\cdot -}$ species. Identifying the champion transition metal

centers of Fe and Ni will be of great help to guide the design of high-performance M–N–C for CO2RR by selectively doping Fe and/or Ni into various nanocarbons architectures, paving a way for realizing an efficient and cost-effective CO_2 -to-fuels process.

In addition, the prepared Ni–N–C exhibited excellent performance in CO_2 reduction with an FE of 96%, a partial current density of -8.2 mA cm^{-2} , a production rate of $0.15 \text{ mmol cm}^{-2} \text{ h}^{-1}$, a TOF of 1060 h^{-1} for CO at a moderate overpotential of 0.65 V, and outstanding electrochemical stability. These results are among the best activities of non-precious catalysts for CO2RR. Owing to its low-cost feedstock and facile preparation, Ni–N–C might be a promising candidate for large-scale CO_2 electrolysis. Therefore, findings in this work could help address the environmental and energy problems associated with the mitigation of CO_2 emissions and the production of sustainable fuels/chemicals.

Acknowledgements

This work was supported by American Chemical Society – Petroleum Research Fund (ACS-PRF #58167-ND10). We thank the Materials Characterization Facility (MCF) at Texas A&M University for providing catalysts characterization resources.

Appendix A. Supplementary data

Supplementary data associated with this article can be found, in the online version, at <https://doi.org/10.1016/j.apcatb.2018.01.001>.

References

- [1] M. Schreier, F. Héroguel, L. Steier, S. Ahmad, J.S. Luterbacher, M.T. Mayer, J. Luo, M. Grätzel, *Nat. Energy* 2 (2017) 17087.
- [2] D.D. Zhu, J.L. Liu, S.Z. Qiao, *Adv. Mater.* 28 (2016) 3423–3452.
- [3] M. Asadi, K. Kim, C. Liu, A.V. Addepalli, P. Abbasi, P. Yasaei, P. Phillips, A. Behranginia, J.M. Cerrato, R. Haasch, P. Zapol, B. Kumar, R.F. Klie, J. Abiade, L.A. Curtiss, A. Salehi-Khojin, *Science* 353 (2016) 467–470.
- [4] Q. Lu, F. Jiao, *Nano Energy* 29 (2016) 439–456.
- [5] W. Zhu, R. Michalsky, Ö. Metin, H. Lv, S. Guo, C.J. Wright, X. Sun, A.A. Peterson, S. Sun, *J. Am. Chem. Soc.* 135 (2013) 16833–16836.
- [6] Q. Lu, J. Rosen, Y. Zhou, G.S. Hutchings, Y.C. Kimmel, J.G. Chen, F. Jiao, *Nat. Commun.* 5 (2014) 3242.
- [7] X. Min, M.W. Kanan, *J. Am. Chem. Soc.* 137 (2015) 4701–4708.
- [8] N. Yang, S.R. Waldvogel, X. Jiang, *ACS Appl. Mater. Interfaces* 8 (2016) 28357–28371.
- [9] L. Dai, Y. Xue, L. Qu, H.-J. Choi, J.-B. Baek, *Chem. Rev.* 115 (2015) 4823–4892.
- [10] D.S. Su, S. Perathoner, G. Centi, *Chem. Rev.* 133 (2013) 5782–5816.
- [11] B. Kumar, M. Asadi, D. Pisasale, S. Sinha-Ray, B.A. Rosen, R. Haasch, J. Abiade, A.L. Yarin, A. Salehi-Khojin, *Nat. Commun.* 4 (2013) 2819.
- [12] A.S. Varela, N. Ranjbar Sahraie, J. Steinberg, W. Ju, H.-S. Oh, P. Strasser, *Angew. Chem.* 127 (2015) 10908–10912.
- [13] F. Pan, A. Liang, Y. Duan, Q. Liu, J. Zhang, Y. Li, *J. Mater. Chem. A* 5 (2017) 13104–13111.
- [14] T.N. Huan, N. Ranjbar, G. Rousse, M. Sougrati, A. Zitolo, V. Mougél, F. Jaouen, M. Fontecave, *ACS Catal.* 7 (2017) 1520–1525.
- [15] C. Zhao, X. Dai, T. Yao, W. Chen, X. Wang, J. Wang, J. Yang, S. Wei, Y. Wu, Y. Li, *J. Am. Chem. Soc.* 139 (2017) 8078–8081.
- [16] J. Shen, R. Kortlever, R. Kas, Y.Y. Birdja, O. Diaz-Morales, Y. Kwon, I. Ledezma-Yanez, K.J.P. Schouten, G. Mul, M.T.M. Koper, *Nat. Commun.* 6 (2015) 8177.
- [17] J. Masa, W. Xia, M. Muhler, W. Schuhmann, *Angew. Chem. Int. Ed.* 54 (2015) 10102–10120.
- [18] H.-W. Liang, W. Wei, Z.-S. Wu, X. Feng, K. Müllen, *J. Am. Chem. Soc.* 135 (2013) 16002–16005.
- [19] J. Wu, F.G. Risalvato, F.-S. Ke, P.J. Pellechia, X.-D. Zhou, *J. Electrochem. Soc.* 159 (2012) F353–F359.
- [20] K.-F. Hsu, S.-Y. Tsay, B.-J. Hwang, *J. Mater. Chem.* 14 (2004) 2690–2695.
- [21] B.J. Hwang, R. Santhanam, D.G. Liu, *J. Power Sour.* 97 (2001) 443–446.
- [22] J. Liu, T. Zhang, Z. Wang, G. Dawson, W. Chen, *J. Mater. Chem.* 21 (2011) 14398–14401.
- [23] F. Pan, J. Jin, X. Fu, Q. Liu, J. Zhang, *ACS Appl. Mater. Interfaces* 5 (2013) 11108–11114.
- [24] A. Fischer, J.O. Müller, M. Antonietti, A. Thomas, *ACS Nano* 2 (2008) 2489–2496.
- [25] P.M. Schaber, J. Colson, S. Higgins, D. Thielen, B. Anspach, J. Brauer, *Thermochim. Acta* 424 (2004) 131–142.
- [26] X. Wang, Y. Zhang, C. Zhi, X. Wang, D. Tang, Y. Xu, Q. Weng, X. Jiang, M. Mitome, D. Golberg, Y. Bando, *Nat. Commun.* 4 (2013) 2905.
- [27] P. Paredes, M.E.H. Maia da Costa, L.F. Zagonel, C.T.M. Ribeiro, F. Alvarez, *Carbon*

- 45 (2007) 2678–2684.
- [28] Z.-H. Sheng, L. Shao, J.-J. Chen, W.-J. Bao, F.-B. Wang, X.-H. Xia, *ACS Nano* 5 (2011) 4350–4358.
- [29] M.-Q. Wang, W.-H. Yang, H.-H. Wang, C. Chen, Z.-Y. Zhou, S.-G. Sun, *ACS Catal.* 4 (2014) 3928–3936.
- [30] W. Niu, L. Li, X. Liu, N. Wang, J. Liu, W. Zhou, Z. Tang, S. Chen, *J. Am. Chem. Soc.* 137 (2015) 5555–5562.
- [31] W. Ding, L. Li, K. Xiong, Y. Wang, W. Li, Y. Nie, S. Chen, X. Qi, Z. Wei, *J. Am. Chem. Soc.* 137 (2015) 5414–5420.
- [32] R. Bhosale, S. Kelkar, G. Parte, R. Fernandes, D. Kothari, S. Ogale, *ACS Appl. Mater. Interfaces* 7 (2015) 20053–20060.
- [33] P. Yin, T. Yao, Y. Wu, L. Zheng, Y. Lin, W. Liu, H. Ju, J. Zhu, X. Hong, Z. Deng, G. Zhou, S. Wei, Y. Li, *Angew. Chem. Int. Ed.* 55 (2016) 10800–10805.
- [34] W. Yao, T. Duan, Y. Li, L. Yang, K. Xie, *New J. Chem.* 39 (2015) 2956–2965.
- [35] D. Guo, Z. Wu, P. Li, Q. Wang, M. Lei, L. Li, W. Tang, *RSC Adv.* 5 (2015) 12894–12898.
- [36] A. Giri, N. Goswami, M. Pal, M.T. Zar Myint, S. Al-Harathi, A. Singha, B. Ghosh, J. Dutta, S.K. Pal, *J. Mater. Chem. C* 1 (2013) 1885–1895.
- [37] M.C. Biesinger, B.P. Payne, A.P. Grosvenor, L.W.M. Lau, A.R. Gerson, R.S.C. Smart, *Appl. Surf. Sci.* 257 (2011) 2717–2730.
- [38] L. Shang, H. Yu, X. Huang, T. Bian, R. Shi, Y. Zhao, G.I.N. Waterhouse, L.-Z. Wu, C.-H. Tung, T. Zhang, *Adv. Mater.* 28 (2015) 1668–1674.
- [39] M. Lefèvre, E. Proietti, F. Jaouen, J.P. Dodelet, *Science* 324 (2009) 71–74.
- [40] H.T. Chung, D.A. Cullen, D. Higgins, B.T. Sneed, E.F. Holby, K.L. More, P. Zelenay, *Science* 357 (2017) 479–484.
- [41] M. Salavati-Niasari, A. Amiri, *Appl. Catal. A: Gen.* 290 (2005) 46–53.
- [42] X. Li, W. Bi, M. Chen, Y. Sun, H. Ju, W. Yan, J. Zhu, X. Wu, W. Chu, C. Wu, Y. Xie, *J. Am. Chem. Soc.* 139 (2017) 14889–14892.
- [43] X. Cui, S. Yang, X. Yan, J. Leng, S. Shuang, P.M. Ajayan, Z. Zhang, *Adv. Funct. Mater.* 26 (2016) 5708–5717.
- [44] Q. Li, P. Xu, W. Gao, S. Ma, G. Zhang, R. Cao, J. Cho, H.-L. Wang, G. Wu, *Adv. Mater.* 26 (2014) 1378–1386.
- [45] L. Zhao, R. He, K.T. Rim, T. Schiros, K.S. Kim, H. Zhou, C. Gutiérrez, S.P. Chockalingam, C.J. Arguello, L. Pálková, D. Nordlund, M.S. Hybertsen, D.R. Reichman, T.F. Heinz, P. Kim, A. Pinczuk, G.W. Flynn, A.N. Paspupathy, *Science* 333 (2011) 999–1003.
- [46] X. Li, H. Wang, J.T. Robinson, H. Sanchez, G. Diankov, H. Dai, *J. Am. Chem. Soc.* 131 (2009) 15939–15944.
- [47] T.-N. Ye, L.-B. Lv, X.-H. Li, M. Xu, J.-S. Chen, *Angew. Chem.* 126 (2014) 7025–7029.
- [48] H. Fei, J. Dong, M.J. Arellano-Jimenez, G. Ye, N. Dong Kim, E.L.G. Samuel, Z. Peng, Z. Zhu, F. Qin, J. Bao, M.J. Yacaman, P.M. Ajayan, D. Chen, J.M. Tour, *Nat. Commun.* 6 (2015) 8668.
- [49] L. Lin, Q. Zhu, A.-W. Xu, *J. Am. Chem. Soc.* 136 (2014) 11027–11033.
- [50] G. Faubert, R. Côté, J.P. Dodelet, M. Lefèvre, P. Bertrand, *Electrochim. Acta* 44 (1999) 2589–2603.
- [51] Y. Zhu, B. Zhang, X. Liu, D.-W. Wang, D.S. Su, *Angew. Chem. Int. Ed.* 53 (2014) 10673–10677.
- [52] Y. Li, W. Zhou, H. Wang, L. Xie, Y. Liang, F. Wei, J.-C. Idrobo, S.J. Pennycook, H. Dai, *Nat. Nanotechnol.* 7 (2012) 394–400.
- [53] J. Xu, Y. Kan, R. Huang, B. Zhang, B. Wang, K.-H. Wu, Y. Lin, X. Sun, Q. Li, G. Centi, D. Su, *ChemSusChem* 9 (2016) 1085–1089.
- [54] W. Li, B. Herkt, M. Seredych, T.J. Bandosz, *Appl. Catal. B: Environ.* 207 (2017) 195–206.
- [55] D. Guo, R. Shibuya, C. Akiba, S. Saji, T. Kondo, J. Nakamura, *Science* 351 (2016) 361–365.
- [56] M. Ma, K. Djanashvili, W.A. Smith, *Phys. Chem. Chem. Phys.* 17 (2015) 20861–20867.
- [57] M. Ma, B.J. Trzeźniowski, J. Xie, W.A. Smith, *Angew. Chem. Int. Ed.* 55 (2016) 9748–9752.
- [58] T. Shinagawa, A.T. Garcia-Esparza, K. Takanabe, *Sci. Rep.* 5 (2015) 13801.
- [59] B.E. Conway, B.V. Tilak, *Electrochim. Acta* 47 (2002) 3571–3594.
- [60] A. Bandi, H.M. Kühne, *J. Electrochem. Soc.* 139 (1992) 1605–1610.
- [61] N. Sreekanth, M.A. Nazrulla, T.V. Vineesh, K. Sailaja, K.L. Phani, *Chem. Commun.* 51 (2015) 16061–16064.
- [62] J. Wu, R.M. Yadav, M. Liu, P.P. Sharma, C.S. Tiwary, L. Ma, X. Zou, X.-D. Zhou, B.I. Yakobson, J. Lou, P.M. Ajayan, *ACS Nano* 9 (2015) 5364–5371.
- [63] Y. Zheng, Y. Jiao, Y. Zhu, Q. Cai, A. Vasileff, L.H. Li, Y. Han, Y. Chen, S.-Z. Qiao, *J. Am. Chem. Soc.* 139 (2017) 3336–3339.
- [64] H. Peng, F. Liu, X. Liu, S. Liao, C. You, X. Tian, H. Nan, F. Luo, H. Song, Z. Fu, P. Huang, *ACS Catal.* 4 (2014) 3797–3805.
- [65] J. Wu, M. Liu, P.P. Sharma, R.M. Yadav, L. Ma, Y. Yang, X. Zou, X.-D. Zhou, R. Vajtai, B.I. Yakobson, J. Lou, P.M. Ajayan, *Nano Lett.* 16 (2016) 466–470.
- [66] D.H. Won, H. Shin, J. Koh, J. Chung, H.S. Lee, H. Kim, S.I. Woo, *Angew. Chem. Int. Ed.* 55 (2016) 9297–9300.
- [67] S. Lin, C.S. Diercks, Y.-B. Zhang, N. Kornienko, E.M. Nichols, Y. Zhao, A.R. Paris, D. Kim, P. Yang, O.M. Yaghi, C.J. Chang, *Science* 349 (2015) 1208–1213.